Occurrence probability of magnetic field disturbances measured with Swarm: Mapping the dynamic magnetosphere-ionosphere coupling

Margot Decotte[1], Karl M. Laundal[1], Spencer M. Hatch[1], Jone P. Reistad[1]

[1]Department of Physics and Technology, University of Bergen, Bergen, Norway

Key Points:

- The disturbed magnetic field occurrence probability is derived from Swarm measurements in the polar regions and investigated statistically
- Low-frequency distributions evince a persistent dawn-dusk asymmetry, peaking at dawn, similar to auroral electron precipitation
- The disturbed magnetic field occurrence probability could, like auroral precipitation observations, be used to infer magnetospheric dynamics

Corresponding author: Margot Decotte, margot.decotte@uib.no

Abstract

The exchange of kinetic and electromagnetic energy by precipitation and/or outflow and through field-aligned currents are two aspects of the ionosphere-magnetosphere coupling. A thorough investigation of these processes is required to better understand magnetospheric dynamics. Building on our previous study using DMSP spectrometer data, here we use Swarm vector field magnetometer data to describe the auroral oval morphology in terms of east-west magnetic field perturbations. We define a threshold for detecting magnetic fluctuations based on the power spectral density of ΔB_{EW}, and derive the disturbed magnetic field occurrence probability (dBOP) at low [0.1–1Hz] and high [2.5–5Hz] frequencies. High-frequency distributions of dBOP reveal a dayside-nightside asymmetry, whereas low-frequency dBOP exhibits a persistent morphological asymmetry between the dawn-to-noon and the dusk-to-midnight sectors, peaking at dawn. Notably, weak solar wind conditions are associated with an increase in the dBOP asymmetric patterns. At low frequency in particular, while the dBOP seems to be primarily constant at dawn, the dusk dBOP decreases during quiet times, inducing a relatively larger dawn-dusk asymmetry in such conditions. We find that the dBOP distributions at low frequencies exhibit features similar to those present in distributions of the auroral electron precipitation occurrence probability, suggesting that the low-frequency dBOP constitutes a reasonable proxy for the large-scale auroral oval. Our interpretation is that the dBOP at low frequencies reflects a quasi-steady state circulation of energy, while the high-frequency dBOP reflects the regions of rapid changes in the magnetosphere. The dBOP is therefore a crucial source of information regarding the magnetosphere-ionosphere coupling.

Plain Language Summary

The Earth's magnetic environment (magnetosphere) and the ionized upper atmosphere (ionosphere) are electrodynamically coupled. Within the magnetosphere-ionosphere (MI) system, energy and momentum are exchanged through both charged and neutral particles. The aurora is one phenomenon resulting from the interaction between solar wind, magnetosphere and ionosphere. While it is commonly thought of as a visual spectacular event, the definition of aurora is broad and all types of aurora are not necessarily visible from the ground. Aurora can also be inferred from satellite data, such as precipitating electron energy flux and magnetic field perturbations. We show that the spatial distributions of these two auroral proxies are similar to the expected large-scale aurora as they both form an oval-shaped region around the magnetic poles. In particular, the auroral oval is persistently wider and/or more intense in the dawn region, compared to dusk. We aim to better understand the MI coupling by investigating the auroral oval morphology through the occurrence probability of disturbed magnetic field.

1 Introduction

Magnetic reconnection at Earth's dayside magnetosphere results in the exchange of plasma populations between the solar wind and the magnetosphere (Dungey, 1961). Following Dungey's cycle, the motion of plasma and the associated convection of magnetic flux within the magnetosphere leads to reconnection in the magnetotail, which in turn excites a flow of accelerated electrons and ions towards the Earth. Solar wind energy and momentum are ultimately transferred from the magnetosphere to the high-latitude ionosphere via the field-aligned currents (FACs), which themselves arise as a response to the stresses applied to the magnetosphere-ionosphere system (Strangeway et al., 2000) and are carried by charged particles flowing along magnetic field lines. FACs have been broadly studied based on observations from low-orbiting satellites, as well as inferred from radars and ground-based magnetometer network observations (e.g., Iijima & Potemra, 1976; Christiansen et al., 2002; Kustov et al., 2000; Kamide et al., 1981). These and many additional studies have established that FACs play a fundamental role in the solar wind-

magnetosphere-ionosphere coupling and, more specifically, auroral physics (Milan et al., 2017).

The auroral oval is commonly described as the high-latitude region where energetic electrons, originally accelerated in the magnetospheric plasma sheet, precipitate (Newell et al., 2004a, 2009; Khazanov & Glocer, 2020). A myriad of studies have focused on auroral particle measurements in the specific context of defining a proxy of the auroral oval. Dombeck et al. (2018), Zhang and Paxton (2008) and Newell et al. (2004b, 2014), for example, derived statistical models of the aurora based on the average precipitating energy flux. In particular, the OVATION Prime model aims at predicting the auroral power deposited in the ionosphere, depending on the solar wind driving. Newell et al. (2009) also contributed to developing auroral precipitation forecasting as they categorized the aurora into diffuse, monoenergetic, broadband, and ion.

Extended knowledge of auroral precipitation has benefited the investigation of the auroral region morphology and dynamics. In their studies, Newell et al. (1996); Redmon et al. (2010); Kilcommons et al. (2017a) derived the auroral oval boundaries based on precipitation data. Recently, Decotte et al. (2023) obtained maps of auroral occurrence probability from precipitating electron energy flux measurements. Furthermore, the expanding-contracting polar cap (ECPC) model predicts the size of the polar cap, depending on the opening and closure of magnetic flux through dayside and nightside reconnection (Cowley & Lockwood, 1992). This, in turn, controls the open-closed boundary (OCB) location, which varies with the amount of open magnetic flux in the magnetotail lobes. Chisham et al. (2022), among others (e.g., Newell et al., 2004b; Kauristie et al., 1999; Carbary et al., 2003; Laundal et al., 2010) have demonstrated that the OCB essentially constitutes the precipitation poleward auroral oval boundary.

In the past decades, it has been extensively shown that a relationship exists between magnetic field perturbations/FACs and particle precipitation. Sato et al. (2004) investigated magnetic field variations and concluded that they were in phase with the high-energy electron flux seen by FAST. Similarly, Hatch, Moretto, et al. (2020) demonstrated the statistical relationship between east-west magnetic field fluctuations and energetic outflows in the magnetosphere-ionosphere transition region. It has also been shown that electron and ion energy flux increase with FACs magnitude in both upward and downward current regions (Robinson et al., 2018). Although they pointed out systematic differences in the location of particle energy fluxes and FACs intensity peak, Xiong et al. (2020) showed that electron and ion energy flux behave in a similar way as FACs, with, in particular, a similar response to enhanced southward B_z.

It has additionally been established in many different studies that magnetic fluctuations and auroral structures were related. Nagatsuma et al. (1995) have found a latitudinally narrow field-aligned current system on the poleward boundary of the nightside auroral oval. They found that this boundary current system is associated with suprathermal electrons with pitch angles predominately in the field-aligned direction. Nagatsuma et al. (1996) further demonstrated that the FAC fluctuations in this boundary current system are due to the superposition of incident and reflected Alfvén waves. Fujii et al. (1985) established that the magnetic fluctuations related well to the fluctuations in auroral luminosities estimated at 100 km altitude. Moreover, Gillies et al. (2015) used Swarm magnetometers to demonstrate the existence of a region of fluctuating field-aligned currents associated with persistent patchy pulsating aurora structures.

Hence, while precipitation studies are crucial in the quest for a better understanding of the auroral region, FACs appear to be a reasonable proxy for the auroral oval. Xiong et al. (2014) have derived auroral oval boundaries from small- and medium-scale FACs and have validated the position of these boundaries against the BAS auroral model derived from IMAGE optical observations. Iijima and Potemra (1978) suggested that FACs sheets are generally aligned with the poleward boundary of the auroral oval, which has

been proven true by Burrell et al. (2020), as they derived the OCB location from the region 1 to region 2 FACs boundary.

The auroral oval is the region of the ionosphere-thermosphere system where the magnetospheric energy converges (Thayer & Semeter, 2004). This convergence of energy results in, among other things, photon emission, Joule heating and satellite drag in the upper atmosphere, and electric currents as well as associated ground magnetic field disturbances (Juusola et al., 2020). A better understanding of the auroral oval dynamics would therefore benefit the MI coupling research and more generally contribute to a better understanding of how the space environment impacts Earth. However, it is challenging to monitor the dynamics of the auroral oval, as this region is highly variable both in space and time (Ohma et al., 2023). All available sensing methods should then be considered when investigating the auroral oval. This study follows a previous investigation of the auroral occurrence probability, using electron precipitation data from DMSP (Decotte et al., 2023). Here we use the Swarm magnetometer data and derive the disturbed magnetic field occurrence probability (dBOP) in the auroral region. This is an alternative to deriving the auroral boundaries directly, which can be ambiguous as it has been shown that the relation between optical observations, ground and space magnetic field measurements, FACs, etc. is complex (Simon Walker's study (A comparison of auroral oval proxies with the boundaries of the auroral electrojets) – paper submitted, waiting for the DOI). Further, when derived from Sun-synchronous satellite observations, modelled boundaries are subject to a local time bias that is bypassed when looking at occurrence probability instead (Decotte et al., 2023). We aim to investigate if the dBOP could be a reliable proxy of the auroral oval.

In Section 2 we introduce the data sets used in this study, which comprise magnetic field and IMF data. We then describe the methodology for deriving the dBOP from magnetic field perturbations. We present the resulting occurrence distributions (maps and MLT profiles) as a function of external conditions such as solar wind driving and substorm activity in Section 3. In Section 4 we summarize the results in terms of morphological features of the auroral oval, and we discuss our findings in relation to the auroral electron precipitation occurrence probability derived in our previous study (Decotte et al., 2023).

2 Data and Methodology

In this section, we present the data used in our study. We also give a detail of the data pre-processing before we introduce the concept of disturbed magnetic field occurrence probability.

2.1 Swarm magnetic field dataset

Our study relies on the measurement of magnetic field perturbations provided by the Vector Field Magnetometer (VFM) carried aboard the Swarm satellites as they cross the polar auroral region. The Swarm constellation mission consists of three identical satellites (A, B and C) in near-polar, circular orbits. Swarm A and C form a pair as they are flying side-by-side (separated by 1.4 degrees in longitude) at approximately 460 km altitude, while Swarm B orbits at a higher altitude of approximately 510 km. All three satellites have an inclination angle of about 87–88 degrees. Such a multi-satellite configuration is well suited to study the current systems of the polar ionosphere (Ritter et al., 2013). We use the virtual research platform – VirES for Swarm – (Smith & Pačes, 2022) to access and collect the high-resolution (50 Hz) magnetic field vector data, which are provided in a local NEC (North-East-Centre) geocentric reference frame. After converting from geocentric to geodetic coordinates, we downsample the Swarm 50 Hz magnetic field vector measurements to 10 Hz by selecting every fifth data point, and we eventually gather all available data from Swarm A and B between 2014 and 2021. We omit

Swarm C in our analysis as Swarm A and C are expected to give similar results due to their proximity and the similarity of their orbital configurations.

As we aim to investigate how the disturbed magnetic field behaves under various geomagnetic conditions, we combine our Swarm dataset with the solar wind magnetic field and plasma parameters from the OMNI database. We point out that these data represent near-Earth estimates of solar wind properties as the original upstream observations have been time-shifted to the Earth's bow shock nose (King & Papitashvili, 2005).

2.2 Data selection procedure

We use the International Geomagnetic Reference Field (IGRF) model to infer the Earth's main magnetic field component for each Swarm data point. We then subtract it from the measured magnetic field, such that only the magnetic field perturbations remain: $\mathbf{B}_{\text{meas}} - \mathbf{B}_{\text{IGRF}} = \mathbf{\Delta B}$. After converting the residual perturbation vector to Apex coordinates (Richmond, 1995), we extract the magnetic field perturbation in the magnetic East-West direction ΔB_{EW}. The selected data should then mostly reflect field-aligned current sheets that run primarily in that direction. The rest of the analysis applies to the portions of the ΔB_{EW} time series falling within $50° \leq |\text{MLat}| \leq 90°$, with MLat in Modified Apex coordinates (Laundal & Richmond, 2017).

2.3 $\mathbf{\Delta B_{EW}}$ spectrograms and spectral power estimates

We use the multitaper method (e.g., Hatch, Haaland, et al., 2020) to derive spectrograms (power spectral density vs frequency and time) from ΔB_{EW} time series. Each power spectrum is calculated from a 20-s window (201 measurements at 10 Hz), and consecutive power spectra are calculated using a 1-s shift. Consequently, given the frequency lower limit (0.05 Hz) and the spacecraft velocity (7.5 km/s), only currents with spatial scales smaller than 150 km are represented. Note that by cutting the 0 Hz frequency we eliminate fluctuations that would otherwise contribute to a similar analysis as done on FACs.

Figure 1 shows an example ΔB_{EW} time series (panel b) and the corresponding spectrogram (panel c) during a Swarm crossing of the polar region (panel a). Note that the spectrogram's y-axis ranges from 0.05 to 5 Hz. The upper limit corresponds to the maximum frequency intended to avoid aliasing in the sub-sampled data (10 Hz). $\Delta B_{EW}(t)$ shows that magnetic field perturbations occur in the vicinity of the auroral region (approximately 68–80° MLat) (panels a and b). Power intensification in the ΔB_{EW} power spectral density (panel c) expresses the presence of fluctuations in $\Delta B_{EW}(t)$, especially at low frequencies (< 0.5 Hz). The dominance of such low frequencies reveals that the power spectral density of ΔB_{EW} mostly features relatively large spatial scale structures (15–150 km).

We eventually calculate the ΔB_{EW} spectral power by integrating the power spectral density over three different frequency ranges in the spacecraft frame of reference: 0.05–0.5 Hz, 0.1–1 Hz, and 2.5–5 Hz. Note that if all observed magnetic fluctuations varied only in space, these frequency bands would respectively correspond to spatial scales of approximately 15–150 km, 7.5–75 km, and 1.5–3 km (see Section 4 for further discussion on this matter). Panel d of Figure 1) shows the three corresponding power time series in cyan, orange and green, respectively.

Performing this procedure for all polar pass data between 2014 and 2021 for Swarm A and B results in about 10^8 measurements that are saved into a database together with their corresponding time and location, to be used in our subsequent statistical analysis.

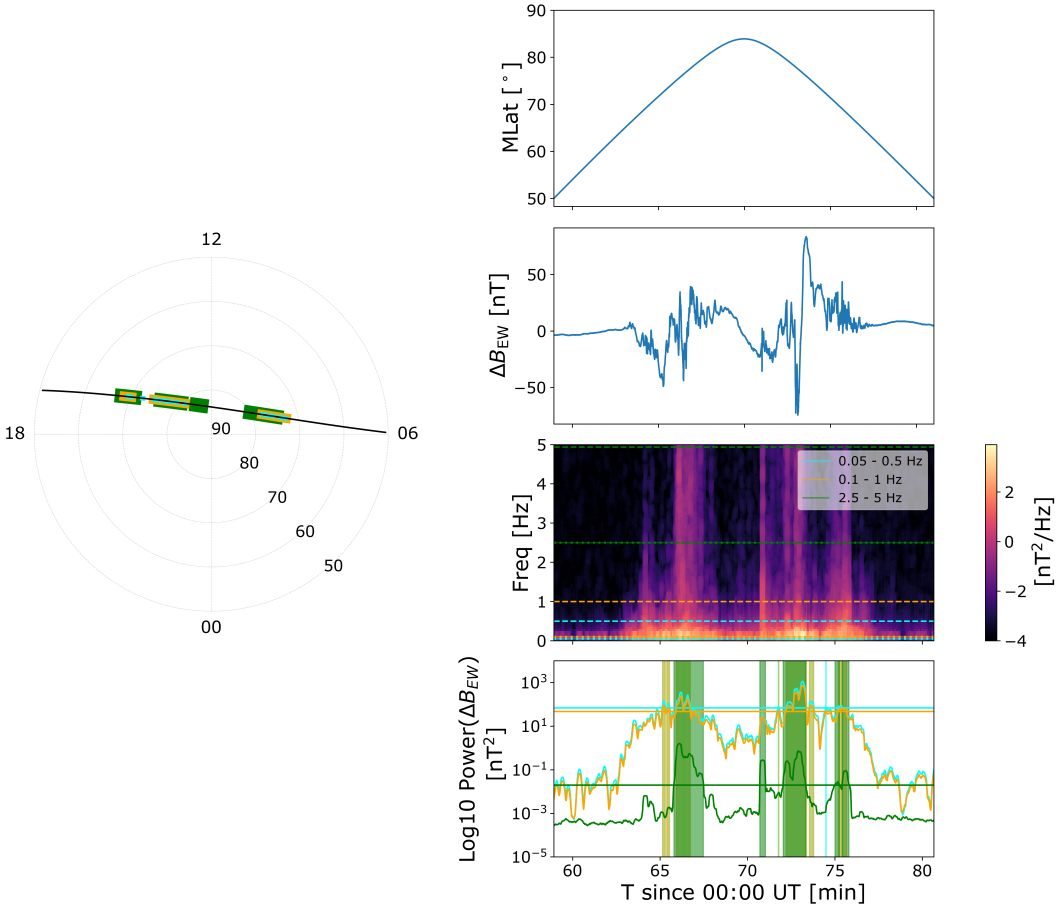

Figure 1: Example disturbed magnetic field identification based on ΔB_{EW} time series from one northern polar region crossing by Swarm A on the 25th of September, 2014, between 00:58:55 and 01:21:00 UT. Left: The spacecraft orbit is shown in black on an Apex magnetic latitude / local time grid. Right, top panel: magnetic latitude of the satellite orbit during this pass. Second panel: Associated ΔB_{EW} time series. Third panel: ΔB_{EW} spectrogram with the frequency on the y-axis and time on the x-axis. The horizontal lines correspond to the lower (dotted) and upper (dashed) limits of different frequency ranges: 0.05–0.5, 0.1–1 and 2.5–5 Hz in cyan, orange and green respectively. Bottom/fourth panel: ΔB_{EW} integrated over each of the previously mentioned frequency bands. The horizontal lines show the threshold for the detection of disturbed magnetic field, within each frequency band. The different regions of detected disturbed magnetic field are shown shaded in cyan, orange or green, depending on the frequency band. The identified regions of disturbed magnetic field are also highlighted in the same color along the satellite orbit (left). This figure can be compared with Figure 2 in Decotte et al. (2023) and Kilcommons et al. (2017b).

2.4 Power threshold for detection of magnetic field fluctuations

We then derive a binary dataset that indicates whether portions of ΔB_{EW} spectral power estimate, within each of the above-mentioned frequency bands, may be deemed to be associated with magnetic field perturbations or not. To generate such a dataset we must define the threshold above which the power estimates are deemed "disturbed magnetic field", and "undisturbed magnetic field" otherwise. This is conceptually similar to the procedure described by Decotte et al. (2023) for producing a binary "aurora/no aurora" time series from DMSP/SSJ electron precipitation measurements. We will discuss how both datasets compare in Section 4.

We choose the magnetic field disturbances detection threshold to correspond to the 75th percentile of the ΔB_{EW} spectral power estimate in each frequency band. This yields power thresholds of 69 nT^2, 48 nT^2 and 0.02 nT^2 for the 0.05–0.5 Hz, 0.1–1 Hz and 2.5–5 Hz frequency bands, respectively. More details about the selection of power limits are given in section 3.1. We will also show that the choice of threshold in a given frequency band has only a minor influence on the conclusions we draw in this study.

Figure 1 (panel d) shows the integrated power spectral density in the 0.05–0.5 Hz, 0.1–1 Hz and 2.5–5 Hz frequency bands in cyan, orange, and green, respectively. The threshold used in each frequency band is represented by the horizontal line of the same colour, such that the spectral power of ΔB_{EW} constitutes magnetic field perturbations when above that limit. The polar plot at left of Figure 1 shows the latitudinal extent of the portions of ΔB_{EW} spectral power exceeding the detection threshold, depending on the frequency band. It can be seen that the high-frequency magnetic field fluctuations (in green) tend to extend to higher latitudes than the lower-frequency structures (in cyan and orange).

2.5 Disturbed magnetic field occurrence probability (dBOP) - Probability of detecting magnetic fluctuations in the auroral region

Still following Decotte et al. (2023), data points from the "disturbed/not disturbed" magnetic field dataset defined in Section 2.4 are binned to an approximately equal-area MLat-MLT grid covering the entire polar regions ($> 60°$ |MLat|). The grid cells are organized in rings of width 1° MLat, with 2 cells in the 89°–90° ring and 68 cells in the 50°– 51° one. We calculate the probability of detecting disturbed magnetic field in each bin (providing that it contains > 200 measurements), by dividing the sum of all observations identified as magnetic field fluctuation by the total number of measurements. In Section 3, we investigate the MLat-MLT distributions of the resulting disturbed magnetic field occurrence probability (dBOP) and its MLT variation under varying external conditions. The MLT profile of dBOP (1D-dBOP) is derived by interpolating the probabilities to a regular MLT-MLat grid (0.5° MLat and 8 min MLT resolution) and averaging the gridded values over latitude. We will see that the 1D-dBOP gives a better sight of potential spatial asymmetries in the disturbed magnetic field than the complete MLat-MLT distribution of dBOP. Note that both hemispheres are combined in all the dBOP distributions presented in the following study, except for the B_y analysis.

3 Results

In this section, we explore the response of the dBOP to intrinsic parameters such as the frequency band and the threshold for magnetic fluctuation detection. We also investigate how the dBOP behaves with respect to various conditions related to IMF orientation and substorm epochs.

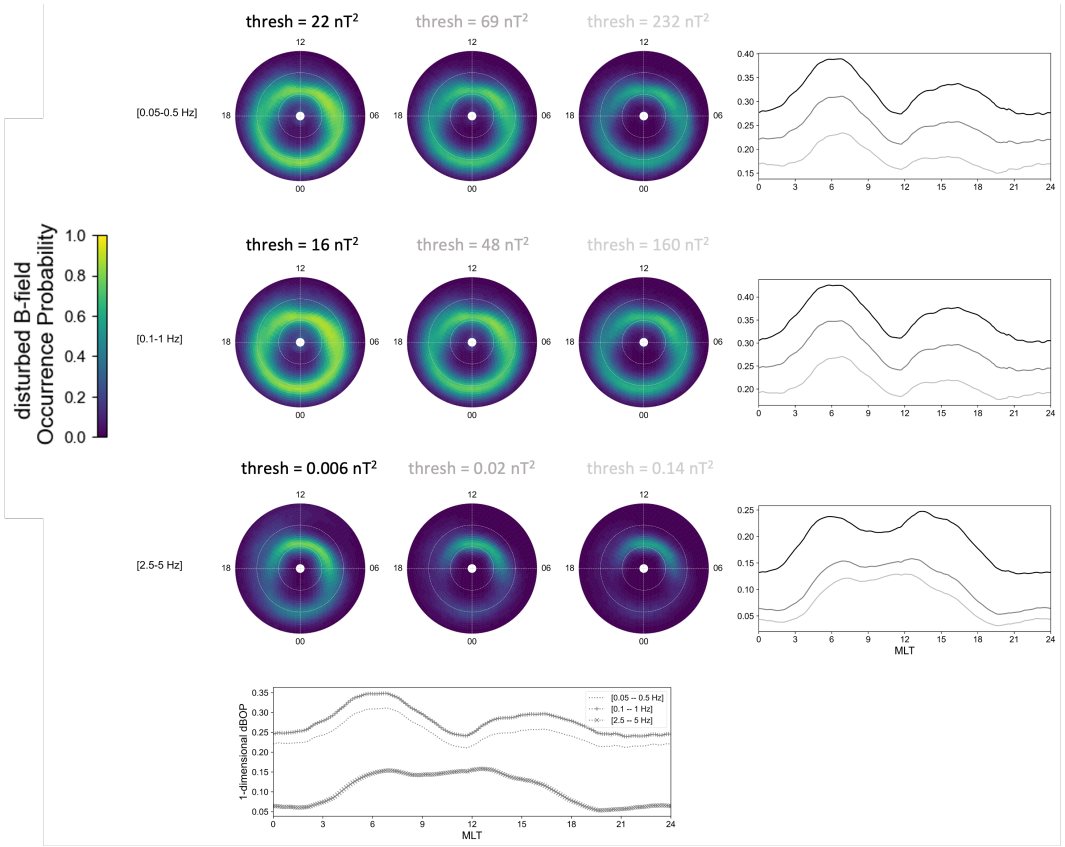

Figure 2: MLat-MLT distributions of dBOP for various frequency bands and thresholds. The top three rows correspond to different frequency bands, while the left three columns illustrate different choices of threshold. From left to right, the thresholds correspond to the 65th, 75th and 85th quantiles of the ΔB_{EW} spectral power estimate in each frequency band. From top to bottom, the frequency bands are as follows: 0.05–0.5 Hz, 0.1–1 Hz and 2.5–5 Hz. The three line plots in the right-most column correspond to the 1D-dBOP derived for all three thresholds, in each of the three frequency bands. The bottom line plot corresponds to the 1D-dBOP derived for the medium-value threshold (2nd column) for all three frequency bands. All distributions presented in this paper span over 60–90° |MLat|, and result from a combination of Swarm A and B observations from both hemispheres (except for the B_y analysis).

3.1 Variation with frequency band and threshold

Figure 2 shows how the dBOP distribution varies depending on the frequency band and threshold for disturbed magnetic field detection. We emphasize that high (green to yellow) values of dBOP correspond to a high probability of detecting a disturbed magnetic field. We also point out that the seven most poleward bins have been neglected since the East-West component of the magnetic field perturbation is unstable near the pole.

The top three rows show the dBOP distributions obtained within three different frequency bands, with each column corresponding to a given threshold. The right-most column shows the MLT profiles (1D-dBOP) obtained for all three thresholds, within a given frequency range. The power thresholds are given by the 65th, 75th and 85th percentiles (from left to right on the figure) of the ΔB_{EW} spectral power estimate in each frequency band. Eventually, the bottom panel shows how the MLT profiles compare between the different frequency bands, using the threshold values corresponding to the 75th percentile. Within a given frequency band, we observe that only the dBOP intensity is affected by the choice of threshold, while the overall distribution morphology is stable. On the other hand, the choice of frequency range can cause major variations in the dBOP distributions. In particular, we expect the high-frequency dBOP distributions to highlight temporal variations in ΔB_{EW} spectral power, while lower frequencies may feature more quasi-static structures.

The dBOP distributions obtained from the two lowest frequency bands 0.05–0.5 Hz and 0.1–1 Hz are highly similar in shape and intensity. They both exhibit an oval shape around the magnetic pole. Regarding the latitudinal range, the low-frequency dBOP essentially spreads between $68 - 80°$ MLat. The 1D-dBOP profiles at these frequencies show two peaks in the dawn (5–8 MT) and dusk (14–18 MLT) sectors, with an asymmetry between these two regions such that the disturbed magnetic field is more often detected at dawn. In contrast, the dBOP distribution obtained from the highest frequency band 2.5–5 Hz exhibits a smaller oval, in particular narrower than the low-frequency dBOP distributions along the dawn-dusk axis. The high-frequency dBOP also has a different asymmetric pattern, with an overall dayside prominence, and a much fainter presence on the nightside. While the dayside peak can be decomposed into two spikes of approximately the same magnitude (at 6 and 15 MLT) in the lower threshold distribution, it tends to flatten for higher thresholds. At such frequencies, and independent of its exact shape, the peak on the dayside probably indicates the importance of directly driven processes as part of the dynamic MI coupling. We discuss this further in Section 4.

Due to the similarity between the two low-frequency bands 0.05–0.5 Hz and 0.1–1 Hz, we pursue our study by restraining the analysis to the 0.1–1 Hz and 2.5–5 Hz intervals. We hereafter refer to these frequency bands respectively as the low- and high-frequency bands. Furthermore, since the choice of threshold for the detection of disturbed magnetic field seems to have no significant influence on the dBOP distribution shape, we will use the intermediate (75th percentile) threshold values 48 and 0.02 nT^2 for the 0.1–1 Hz and 2.5–5 Hz frequency bands, respectively.

3.2 Comparison with average power

Figure 3 (low-frequency) and Figure 4 (high-frequency) show the dBOP (left) and the median power distributions (right) for northward (top) and southward (bottom) IMF. The peak in dBOP is defined as dBOP values exceeding 0.85 (low-frequency) or 0.5 (high-frequency) and is shown as red dots on the left maps. The comparison between both types of distributions for given geomagnetic conditions reveals that the dBOP behaves distinctly from the average power.

Figure 3 shows that, at low frequencies, the dBOP exhibits a dayside peak (7–15 MLT) in the low geomagnetic activity (B_z positive) distribution. The low-frequency av-

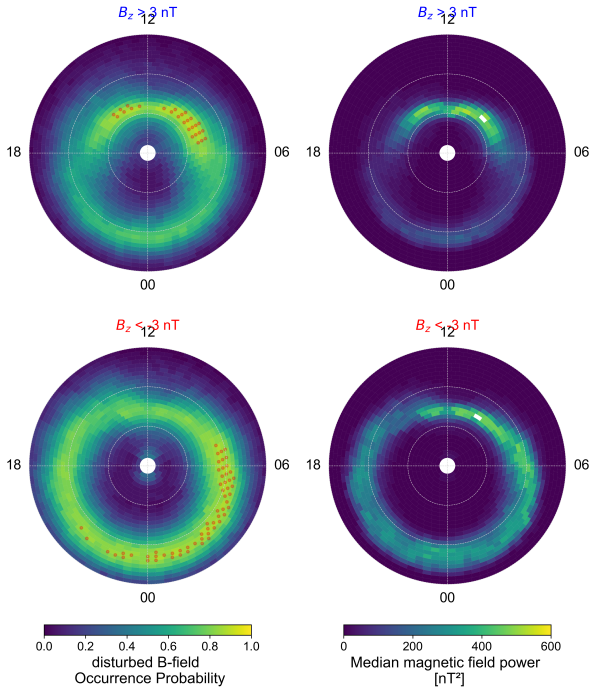

Figure 3: Distributions of low-frequency [0.1–1 Hz] magnetic field fluctuation occurrence probability (left) and median magnetic field power (right) for positive (top) and negative (bottom) IMF B_z. The red dots on the left maps indicate bins with dBOP value > 0.85 (dBOP peak).

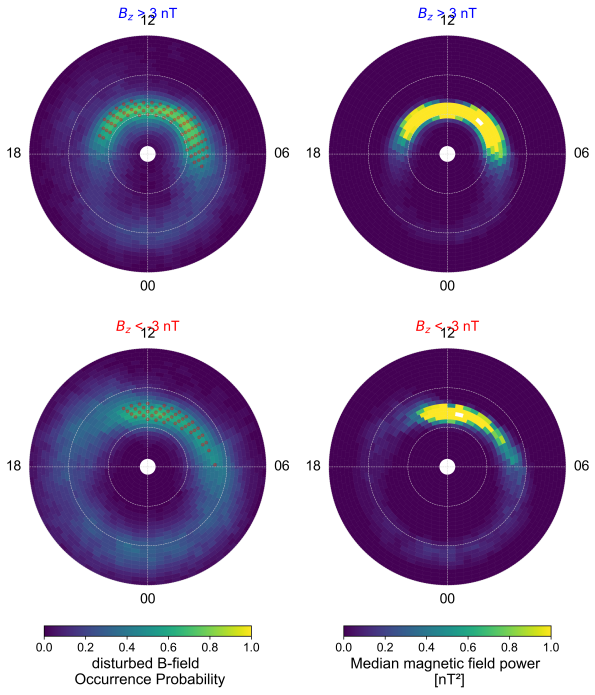

Figure 4: Similar as Figure 3, but for high frequencies [2.5–5 Hz]. The red dots on the left maps indicate bins with dBOP value > 0.5 (dBOP peak).

erage power also displays a clear peak on the dayside but the rest of the oval is much fainter than the dBOP everywhere else. Still at low frequency, increased geomagnetic activity (B_z negative) leads both types of distributions to expand to lower latitudes on the nightside. In terms of intensity, the dBOP peaks all the way from pre-midnight to the dawn sector (22–8 MLT) during such disturbed times. The increase in the average power is significant in all MLT sectors from 17 to 7, but the dawn-to-noon region remains the most intense. Thus, the peak sector in dBOP overlaps with the average power peak only in a narrow region around 6–7 MLT.

Distinct observations can be made from Figure 4 at high frequencies. Here, the dBOP and average power distributions vary in the same fashion. In particular, they are globally very faint in all MLT sectors except on the dayside, for both quiet and active times. The effect of enhanced geomagnetic activity is scarcely visible, resulting in broader but still very spread dBOP and average power distributions, with narrower regions of peak intensity compared to lower geomagnetic activity. As opposed to the low-frequency distributions, the peak regions in the dBOP at high frequencies and in the average power are coincident and located in the 8–13 MLT region.

The correlation between high-frequency dBOP and average power might be another indication that the dBOP, at such frequencies, is an image of the strong/dynamic coupling between the magnetosphere and ionosphere. With this assumption, the dayside peak in the dBOP would then reflect a region in the ionosphere that is directly coupled to the solar wind. On average, changes in the IMF and the subsequent reconnection at the magnetopause trigger magnetic field activity in a definite region on the dayside, thus resulting in a peak in both the dBOP at high frequencies and the average magnetic field power. During increased geomagnetic activity ($B_z < 0$), the forcing at the magnetosphere is stronger but the region of coupling on the dayside becomes more variable and results in a larger but more diffuse region of disturbed magnetic field, as seen in both types of distributions. The same phenomenon applies to the nightside, where, on average, reconnection occurs over a much larger region in space – compared to the dayside – thus resulting in a faint distribution in both the high-frequency dBOP and the average magnetic field power.

3.3 Variation with IMF Bz

Figure 5 (low-frequency) and Figure 6 (high-frequency) show the variation of dBOP with solar wind driving. Both MLat-MLT distributions (maps) and MLT profiles (line plot) of the dBOP are shown. The maps are a repetition of the distributions presented in Figures 3 and 4, hence we mostly focus on the analysis of the 1D-dBOP in this paragraph.

Figure 5 highlights the asymmetric pattern in the low-frequency dBOP distributions. During quiet times (left map, blue profile), there is an overall dayside prominence with two peaks at around 6 and 16 MLT. The distribution peaks in the dawn sector (4–7 MLT) and reaches a minimum in the dusk-to-midnight region (21–00 MLT). An increase in solar wind driving (right map, red profile) leads to a broadening of the dBOP oval as well as its expansion to lower latitudes. Such change in the dBOP is particularly visible in the nightside (18–6 MLT). As a consequence, the relative asymmetry between dawn and dusk is dramatically reduced for negative B_z, although the dawn sector still dominates the distribution. Figure 6, on the other hand, does not exhibit any specific asymmetric pattern between the dawn and dusk sectors. It shows that the dBOP distributions at high frequencies are dominated by the dayside sector (particularly the cusp region), independent of the sign of B_z. Enhanced solar wind driving results in an overall larger but more diffuse distribution, as well as a shift to lower latitudes for the prenoon-cusp sector. We emphasize that these distributions show the same dependence on IMF B_z as the small-scale FACs derived in Neubert and Christiansen (2003), both in terms

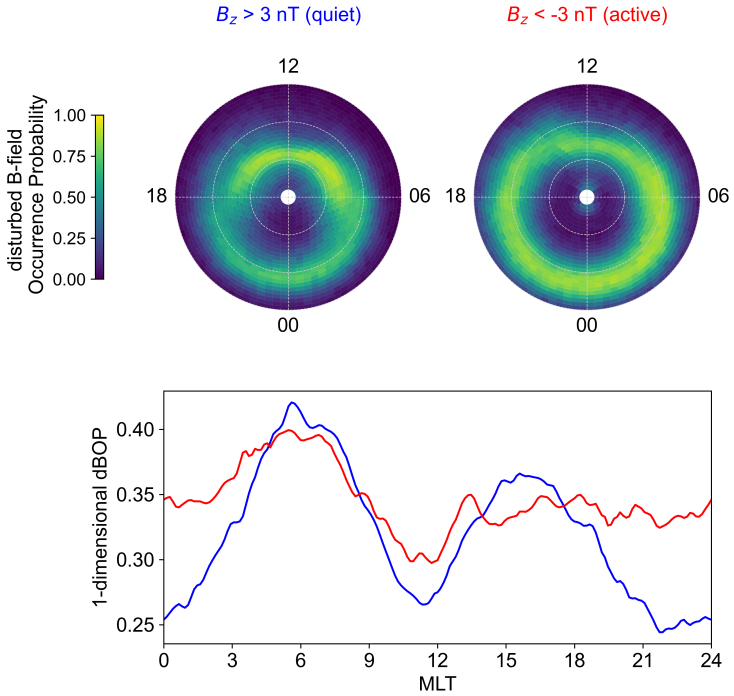

Figure 5: MLat-MLT distributions of low-frequency [0.1–1 Hz] dBOP (top row) and MLT profiles of 1D-dBOP for IMF B_z positive (left, blue) and B_z negative (right, red)

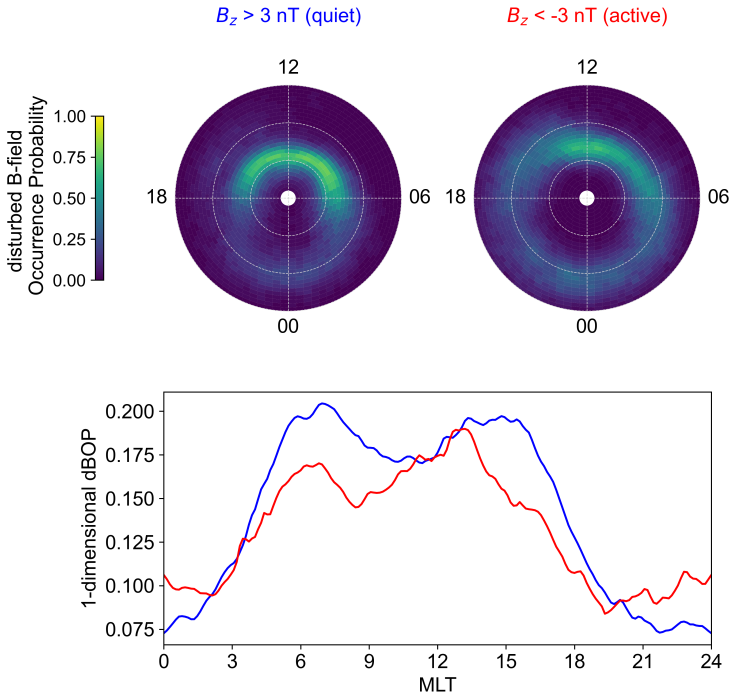

Figure 6: Similar as Figure 5, but for high frequencies [2.5–5 Hz].

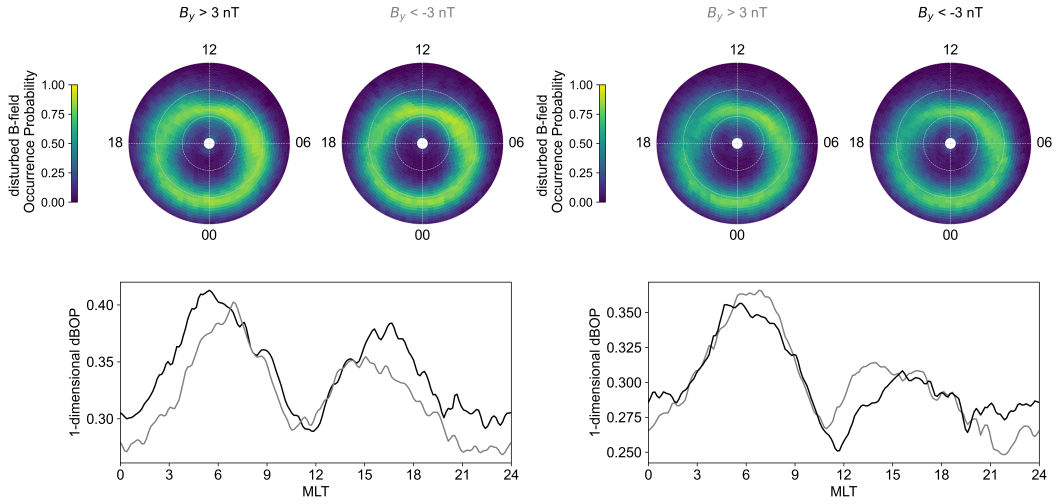

(a) Northern Hemisphere

(b) Southern Hemisphere

Figure 7: MLat-MLT distributions of low-frequency [0.1–1 Hz] dBOP and MLT profiles of 1D-dBOP for different IMF B_y orientations, for the Northern (left) and Southern (right) Hemispheres. For inter-hemispheric comparison, B_y positive (negative) in the Northern Hemisphere is often assumed to correspond to B_y negative (positive) in the Southern Hemisphere (Hatch et al., 2022).

of peak location and intensity. Additionally, an increase in the geomagnetic activity leads to a slight increase of the dBOP distribution on the nightside and simultaneously a small decrease on the dayside, which tends to reduce the dayside-nightside asymmetry during such active times ($B_z < 0$). A common feature between low and high frequencies is thus a decrease of the asymmetry in the dBOP distribution during active geomagnetic times, although the asymmetric patterns are different.

3.4 Variation with IMF By

We compare the dBOP distributions (maps and MLT profiles) for different orientations of IMF B_y. Figures 7a and 7b show the low-frequency dBOP variation with B_y for each hemisphere. Figures 8a and 8b present the same analysis but for high frequencies.

The MLT profiles of dBOP in Figure 7 (low-frequency) reveal inter-hemispheric asymmetries: the dBOP distribution for B_y positive in the Northern Hemisphere varies differently than the dBOP for B_y negative in the Southern Hemisphere (black lines), relatively to the dBOP distribution for the opposite B_y (grey lines) in each hemisphere. The difference between North and South mainly lies in the post-midnight (3–5 MLT) and in the postnoon-to-dusk (12–19 MLT) sectors. In the Northern Hemisphere, positive B_y (black line) gives higher values of 1D-dBOP compared to B_y negative (grey line) at all MLTs except in the post-noon sector where both distributions are equivalent. In the Southern Hemisphere, negative B_y (black line) gives higher values of 1D-dBOP than B_y positive (grey line) only on the nightside (20–3 MLT). In other MLT sectors, distributions of dBOP for both B_y signs are either equal (dawn, prenoon and dusk sectors) or the distribution for $B_y > 0$ is greater than the distribution for $B_y < 0$ (6–9 and 11–15 MLT). In terms of intensity, the Southern Hemisphere displays lower values of 1D-dBOP than

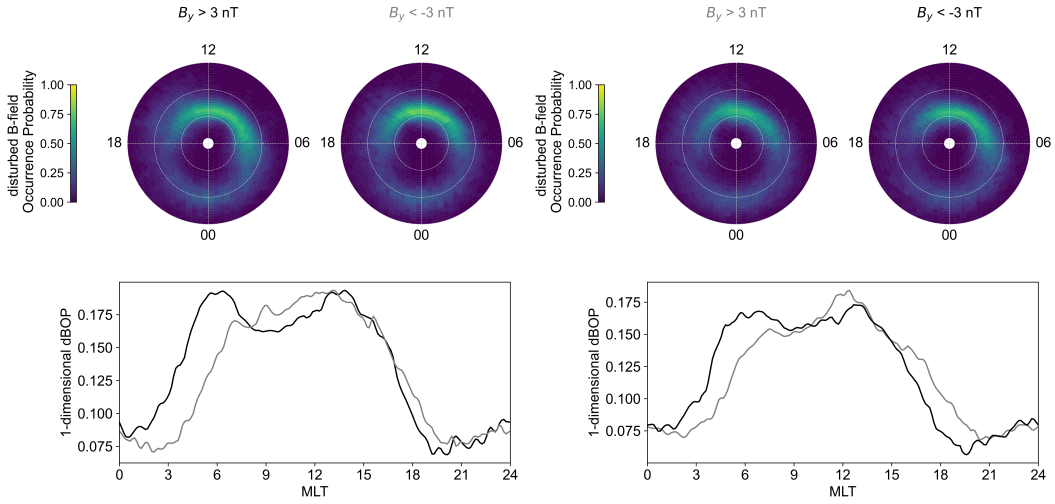

(a) Northern Hemisphere

(b) Southern Hemisphere

Figure 8: Similar as Figure 7, but for high frequencies [2.5–5 Hz].

the Northern Hemisphere for both B_y orientations in all MLT sectors, which might have to do with strength differences in the main magnetic field itself. Despite these divergences, the dawn-dusk asymmetry is present in the low-frequency dBOP for both hemispheres and both B_y orientations. However, while it seems to be independent of the B_y sign in the Northern Hemisphere, the asymmetric pattern is slightly reduced for By negative (in black), compared to By positive (in grey), in the Southern Hemisphere.

Figure 8 shows that the dBOP behaviour with B_y orientation at higher frequencies is different from the behaviour observed at low frequencies. Here, the 1D distributions obtained for B_y positive and negative in the Northern Hemisphere essentially match the distributions for B_y negative and positive in the Southern Hemisphere. In particular, the MLT profiles of dBOP for both B_y signs are almost identical on the nightside, in both hemispheres. In the Northern Hemisphere, the values of 1D-dBOP for positive B_y (in black) exceeds the 1D-dBOP obtained for the opposite B_y orientation (in grey) at dawn, and this trend is reversed around the noon region and at dusk. The same applies in the Southern Hemisphere, where the dBOP distribution for negative B_y (in black) also exceeds the distribution obtained for the opposite B_y orientation (in grey) at dawn, with a reversed trend around the noon region and at dusk.

Figures 7 and 8 show that independent of hemisphere or the sign of B_y, the dBOP distributions presented here are relatively similar to the distributions previously described in this study (see sections 3.1 and 3.3). As opposed to its strong influence on FACs, the effect of B_y orientation on dBOP is thus overall weak as the global shape of dBOP is conserved. In particular, the asymmetric pattern (between dawn and dusk at low frequencies and between dayside and nightside at higher frequencies) remains the main morphological characteristic in the dBOP distributions. We therefore assume the inter-hemispheric differences reported here to have no major consequence on the conclusions we draw in this study (as they mostly have to do with the persistent asymmetric pattern in dBOP), such that both hemispheres can be safely combined in the rest of the analysis.

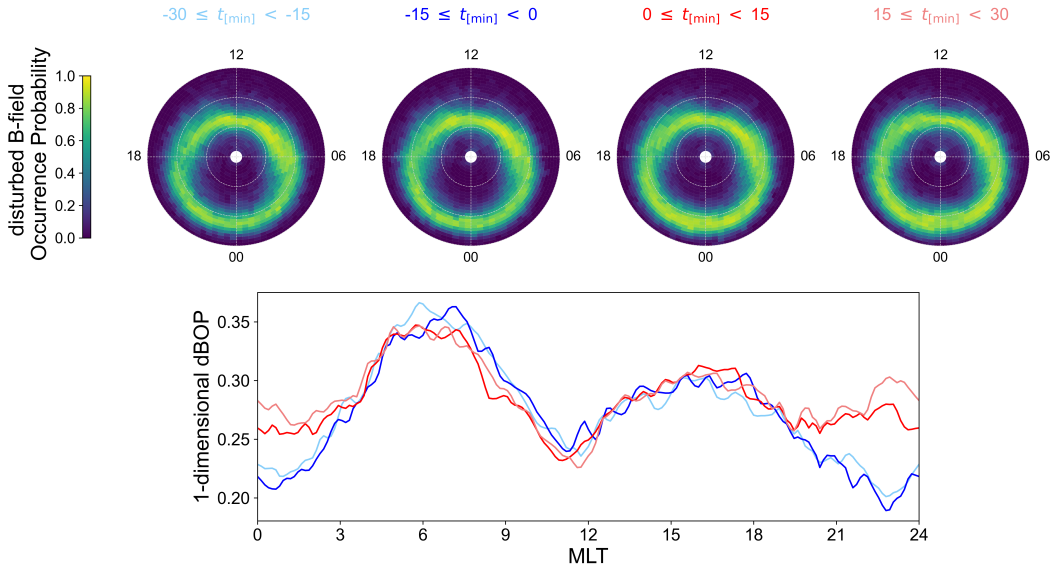

Figure 9: Low-frequency [0.1–1 Hz] dBOP distributions (top row) and MLT profiles of 1D-dBOP (bottom panel) for four different 15 min-time ranges around substorm onset. From left to right the time ranges are respectively -30 min $\leq \ t \ < -15$ min (light blue), -15 min $\leq t < 0$ min (dark blue), 0 min $\leq t < 15$ min (dark red), 15 min $\leq t < 30$ min (light red).

3.5 Variation with substorm epochs

In this section, we aim to determine how the disturbed magnetic field occurrence probability varies throughout the substorm cycle. We use the Ohtani and Gjerloev list of substorm onsets identified from the SuperMAG SML index (Ohtani & Gjerloev, 2020).

Figures 9 (low frequencies) and 10 (high frequencies) show the statistical evolution of the dBOP MLat-MLT distribution with the substorm cycle, and the corresponding MLT profiles of 1D-dBOP, from 30 min before substorm onset ($t = 0$) up until 30 min after onset (in blue and red, respectively), separated into 15-min intervals.

The dBOP global morphology remains unchanged and similar to the dBOP distributions previously described in this study. In particular, the MLT profiles in Figure 9 and 10 exhibit the usual dawn-dusk asymmetry in the low-frequency dBOP, and the asymmetry between dayside and nightside in the high-frequency dBOP. In both frequency bands, the influence of substorm phases on these distributions is mainly visible on the nightside. In the pre-midnight sector (21–23 MT), the 1D-dBOP distributions indicate a sharp increase in the probability of detecting disturbed magnetic field after substorm onset. This can also be observed in the MLat-MLT distributions (maps) as a small expansion/intensification of the dBOP oval around midnight. The after-onset dBOP then stays higher than before onset from about 21 to 3 MLT. In all other MLT sectors, the dBOP remains unchanged for $t < 0$ and $t > 0$. Despite the significant increase in dBOP on the nightside, the four low-frequency dBOP distributions still peak at dawn and the high-frequency dBOP still presents a broad peak from 6–13 MLT, independent of the substorm epoch. Hence substorm onsets tend to reduce the asymmetric pattern in the dBOP distributions, in a similar way as the rise in geomagnetic activity associated with southward IMF B_z for example (see section 3.3).

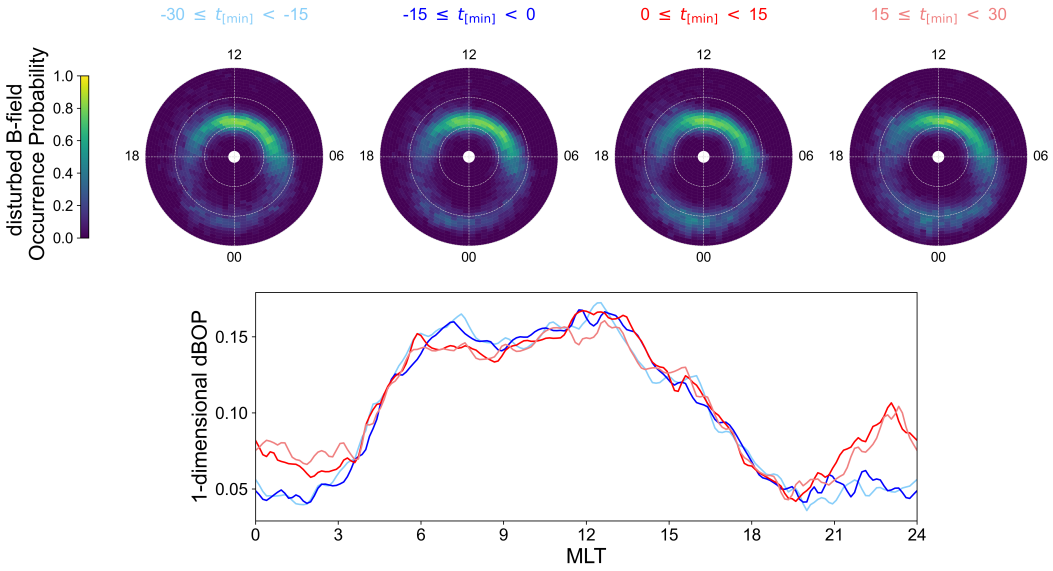

Figure 10: Similar as Figure 9, but for high frequencies [2.5–5 Hz].

4 Discussion

We used Swarm ΔB_{EW} measurements to derive MLat-MLT maps of the disturbed magnetic field occurrence probability for different conditions. In this section, we discuss methodology limitations resulting from the ambiguity between spatial and temporal variations as it is complex to determine whether the spacecraft is moving through quasi-static structures or if the structures themselves are dynamic. We also compare the dBOP with auroral boundaries derived from FAC signatures and finally discuss the connection between the dBOP and the auroral oval.

4.1 Interpretation of magnetic field variations in the satellites' moving frame of reference

We found important discrepancies between the low- and high-frequency dBOP distributions. At high frequencies, the dBOP distributions essentially highlight the dayside and, to a lesser extent, the midnight sector. As they directly map to active regions in the magnetosphere (regions of reconnection on the dayside and depolarization on the nightside), such sectors are subject to strong forcing when there is a stress imbalance between the ionosphere and the magnetosphere. Thereby, high-frequency magnetic field perturbations are commonly associated with dynamic FACs (typically Alfvén waves), which are generated in response to the tension on the magnetic field lines. On the other hand, the low-frequency dBOP is generally more spread over all MLTs. Indeed, low-frequency magnetic field perturbations indicate a more balanced stress between the ionosphere and magnetosphere, associated with quasi-steady-state FACs. Such perturbations are expected to reflect the average ionospheric current patterns, such as those described by the Average Magnetic Field and Polar Current System (AMPS) model (Laundal et al., 2018).

Consequently, in terms of magnetic field fluctuations, the low-frequency dBOP is more likely to relate to large-scale spatial variations while the high-frequency dBOP is expected to reflect temporal variations. However, we emphasize that the magnetic field disturbances measured by Swarm cannot be unambiguously identified as either spatial or temporal variations. This is due to the discrepancy between the Doppler-shifted fre-

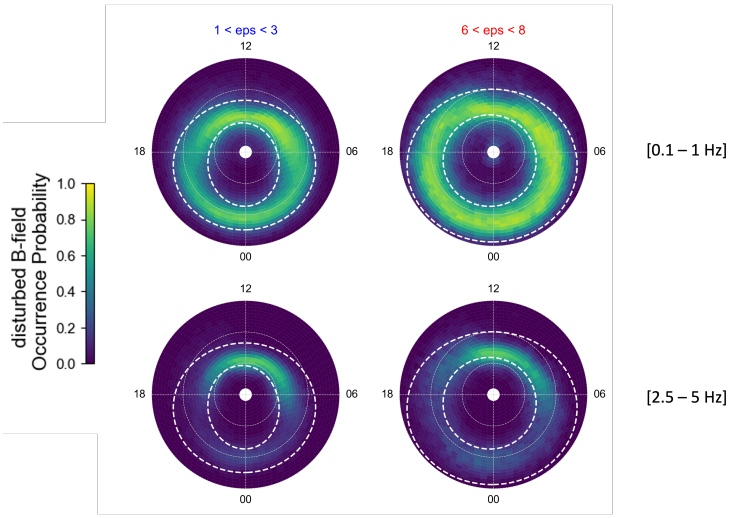

Figure 11: Low- [0.1–1 Hz] (top) and high-frequency [2.5–5 Hz] (bottom) dBOP distributions for low (left) and high (right) solar wind driving based on two different ranges of the Newell coupling function; namely [1–3] and [6–8]. Auroral oval boundaries – as derived from the Xiong et al. (2014) model – are shown as the white dashed line on top of each distribution and correspond to an epsilon value of 2.5 (low solar wind driving, left) and 5.45 (high solar wind driving, right) respectively

quency of the wave observed in the satellite reference frame and the wave frequency in the plasma reference frame (Stasiewicz et al., 2000; Chaston et al., 2004). Nonetheless, even in an ideal quasi-static scenario, it is challenging to assert whether the detected variations are purely spatial or not. The reason for that is that we have no information about the orientation of the current sheet the spacecraft is flying through. For example, for satellite orbits that do not cross circles of latitude perpendicularly, a structure oriented east-west in magnetic coordinates will take longer to traverse and appear as lower frequencies (larger in space) than the same structure if crossed perpendicularly. This bias towards low frequencies might occur more often in the Southern Hemisphere than in the Northern Hemisphere due to the wider orbital plane in magnetic coordinates caused by the offset between magnetic and geographic poles – this offset being larger in the South.

Yet, despite the space-time ambiguity, we found that the high-frequency dBOP behaves similarly to small-scale FACs (Neubert & Christiansen, 2003) (see Section 3.3). Additionally, we now compare our dBOP distributions with the Xiong and Lühr auroral oval boundaries (Xiong & Lühr, 2014) which are derived from small and medium-scale CHAMP field-aligned current signatures. The Xiong and Lühr (2014) model is such that the position of the poleward and equatorward boundaries are fitted by ellipses that are parameterized by the Newell coupling function (merging electric field), which quantifies the solar wind input into the magnetosphere (Newell et al., 2007). Figure 11 shows the low- and high-frequency dBOP distributions for low and high solar wind driving conditions, with the modelled boundaries plotted on top (white dashed). Note that Xiong and Lühr (2014) used a time-integrated version of the merging electric field (Equation (2) in their paper), while our dBOP distributions are simply derived from the original Newell coupling function (Equation (1) in the same paper). As a first approximation, these figures indicate a good agreement between dBOP and Xiong et al. (2014) auroral boundaries, as the regions of intense dBOP (> 0.6) are plainly enclosed by the boundaries. At low frequencies, in particular, the correspondence is excellent. At high frequencies, the boundaries tend to delimit a much larger oval than the dBOP, but still give an approx-

imate idea of the location of the high-frequency dBOP oval. Moreover, the modelled boundaries exhibit a modest dawn-dusk asymmetry. This is marginally visible along the 6–18 MLT meridian, and more evident when looking along the $\sim$ 9–21 MLT meridian. Although less pronounced than the asymmetry in the corresponding dBOP distributions, this is another indication that the auroral oval boundaries derived by Xiong et al. (2014) and the dBOP display similar features.

Regardless of the ambiguous space-time interpretation, we demonstrated a relatively good match between dBOP distributions and the modelled boundaries derived by Xiong et al. (2014). In particular, the low-frequency dBOP adequately captures where the auroral zone FACs are located. The rest of the discussion focuses on the relation between dBOP and auroral oval.

4.2 Relation with the auroral oval - Magnetic field version of the precipitation occurrence probability

In a previous study, we derived the electron precipitation occurrence probability (POP) from precipitating electron energy flux measurements at high latitudes (DMSP/SSJ) (Decotte et al., 2023). We established a direct connection between the electron precipitation and the probability of observing aurora by setting an energy flux threshold above which the electron energy flux (in the energy range 1–30 keV) is assumed to result in auroral features (Kilcommons et al., 2017b). One of the main findings from the POP study was the asymmetric pattern of the auroral occurrence oval, with a persistent preference for the dawn side compared to dusk. In the present study, we follow a similar method to derive the dBOP, which quantifies the probability of detecting magnetic field fluctuations in space above the polar region. As described in Section 2, the magnetic field spectral power is classified as either "disturbed" or "undisturbed" based on the examination of magnetic field perturbations in different frequency bands. As a first-order approximation, we showed that the dBOP exhibits an oval shape around the magnetic poles, revealing asymmetries between MLT sectors. These similarities motivate the investigation of a possible relationship between dBOP and POP. Therefore, while we performed the analysis without any assumption related to the precipitation auroral oval (see Section 3), this section is an attempt to explain our dBOP distributions in the context of auroral precipitation. We further discuss the potential use of dBOP as a proxy for the average auroral oval.

Figure 12 shows how the dBOP MLat-MLT distributions at low (top left map) and high (top right map) frequencies compare to the POP (bottom map), using our entire data sets (no specific selection regarding geomagnetic conditions). The corresponding MLT profiles are also shown, with the 1D low- and high-frequency dBOP in orange and green on the bottom panels at left and right, respectively. The 1D-POP is plotted on top of each panel as the black line. We emphasize that the local time coverage is one major difference between POP and dBOP distributions. While DMSP (POP) does not cover the postnoon and postmidnight sectors, Swarm data (dBOP) have the benefit of relatively even coverage of all local times during all seasons (Lühr et al., 2019).

On the one hand, the auroral ovals revealed by the low-frequency dBOP and the POP in Figure 12 exhibit similarities in shape and location - especially at the poleward boundary - such that the preferential MLat-MLT region for magnetic fluctuations and the preferred region for auroral electron precipitation seem to be, at first order, related. Although comparable to some extent, both ovals have different latitudinal extents, with overall smaller 1D-dBOP amplitudes (MLT profiles) compared to the POP. This feature is well identified by the comparison plot between the dBOP and POP MLT profiles (left panel of Figure 12), which also highlights the weaker dawn-dusk asymmetry in the dBOP (in orange) compared to the POP (in black). On the other hand, dBOP and POP significantly differ at higher frequencies. There is no longer dawn-dusk asymmetry in the

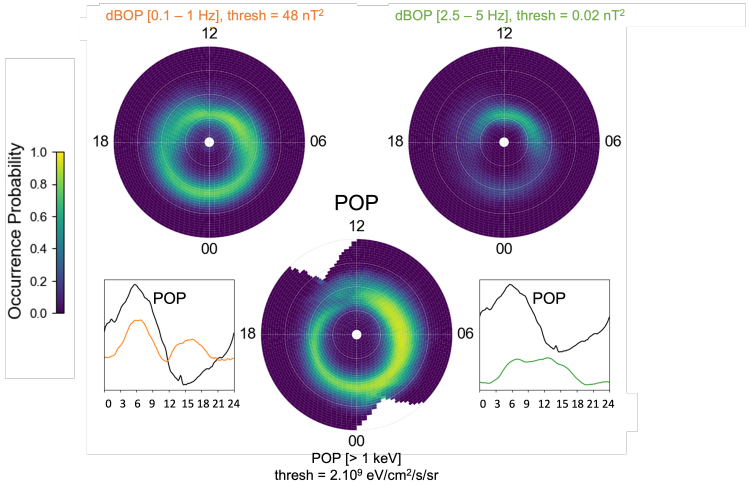

Figure 12: Comparison between dBOP (top maps) at low (left map, orange profile) and high (right map, green profile) frequency, and POP (bottom map, black profile). Both types of distributions are presented over the same latitudinal range $50° \leq |\text{MLat}| \leq 90°$.

dBOP oval at such frequencies, only a broad peak on the dayside (6–16 MLT), with very faint probabilities everywhere else. As a consequence, the dominant morphological patterns in dBOP and POP are highly contrasting in these conditions, as indicated by the associated MLT profiles (right panel of Figure 12, dBOP in green and POP in black).

We also looked at the response of the dBOP distributions to the level of geomagnetic activity (orientation of IMF B_z and time relative to substorm epoch, see Sections 3.3 and 3.5) and found that, independent of the frequency band, the MLT asymmetry is decreased during active times, due to a considerable enhancement in the dBOP in the nightside sector. This tendency is also observed with the dawn-dusk asymmetry in the POP distributions in Decotte et al. (2023). We emphasize that although the variation of geomagnetic activity impacts the degree of asymmetry in the dBOP and POP distributions in a similar fashion (the more active, the less asymmetric), the asymmetry in the dBOP is reduced to a larger extent than the POP during disturbed geomagnetic times. A quick comparison between the POP and dBOP responses to a southward turning of the IMF or to substorm onset shows that there is a relative lack of response of the POP, while the dBOP distributions are more impacted by such increased activity (greater nightside activation). This partly explains the larger asymmetric pattern in the POP, compared to the dBOP.

In Decotte et al. (2023), we proposed a theory to explain the dawn-dusk asymmetry observed in the POP. The argument relies on a fluid description in which we assume a topological mapping between the auroral oval and the magnetospheric plasma sheet, such that variations in the amount of closed magnetic flux induce similar variations in the auroral region. We showed that the Earth's corotation influence on the plasma convection pattern could be partly responsible for the auroral oval asymmetric shape. Since the low-frequency dBOP and the POP appear to be analogous, this approach could still be valid and partially explain why the dBOP morphology is dominated by an asymmetric pattern between the dawn and dusk sides of the auroral region. In particular, connecting the dBOP to this perspective fits the idea that the auroral oval's shape is not only regulated by energetic precipitation but also depends on the magnetic coupling between the magnetosphere and ionosphere. Moreover, in this picture, it is expected that low- and high-frequency dBOP behave in a different manner. We showed that at high

frequencies the dBOP mainly reflects ionospheric regions that are related to dynamic changes in the magnetosphere. These regions are not influenced by the Earth's rotation, unlike the large-scale plasma convection associated with the more steady MI coupling. This could consequently explain the lack of dawn-dusk asymmetry in the high-frequency dBOP.

Kilcommons et al. (2017b) have produced maps of the large-scale FACs derived from DMSP magnetometer (SSM) data and compared where the R1 and R2 current systems lie relative to the electron precipitation boundaries, as derived from DMSP SSJ data. They found a dawn-dusk asymmetry in the FAC location, with higher latitude FACs in the dawn region compared to dusk. This latitudinal feature compares well with our low-frequency dBOP distributions derived for different levels of geomagnetic activity (see Sections 3.3 and 3.5). However, the asymmetric pattern they point out doesn't necessarily translate into a wider or more intense dBOP region at dawn. But interestingly enough, they interpret it as related to the extent of the region of strong precipitating electron flux and point to the constantly wider dawn side auroral region. Thereby, this asymmetry in the auroral region is a recurrent pattern in the electron precipitation auroral oval, the field-aligned currents and the disturbed magnetic field at low frequency.

It makes sense, based on what we know about ionospheric electrodynamics, that the low-frequency dBOP (indicative of quasi-steady FACs) and POP (which essentially reflect the large-scale long-term pattern of the auroral oval) are related. Steady-state FACs are well described by the ionospheric Ohm's law and depend on conductance, which is partly controlled by particle precipitation. Moreover, it is commonly known that auroral precipitation increases the ionospheric conductance in the same region as where the R1/R2 FACs are located (Milan et al., 2017). It then appears plausible that the low-frequency dBOP may be part of the signature of the diffuse auroral precipitation presented in Decotte et al. (2023). On the other hand, the high-frequency dBOP relates more to the propagation of Alfvén waves. On the dayside, there is a noteworthy resemblance between the range of MLTs over which the high-frequency dBOP is enhanced and the range of MLTs over which statistical distributions of inertial Alfvén wave Poynting flux are enhanced for both positive and negative B_y orientations (Figure 2a in Hatch et al., 2017). In addition, as Alfvén waves can cause the acceleration of charged particles and their precipitation into the auroral zone, it is expected that the high-frequency dBOP might be more similar to either monoenergetic or broadband aurora than to diffuse aurora (Newell et al., 2009). It is therefore useful to compare the maps from Figure 12 in Newell et al. (2009), showing the occurrence probability of broadband acceleration of precipitating particles, with the dBOP distributions from Figure 6 (B_z analysis). This comparison indicates a good match between the peak regions. During low solar wind driving, the probability of observing broadband acceleration is restrained to two hot spots, the main one being in the dawn sector and the other one in the post-noon MLT region. This compares with the high-frequency dBOP during quiet times ($B_z > 0$), which also peaks in the dawn-to-noon sector, with, however, a high-probability region covering the entire dayside. In particular, an important difference with Newell's electron precipitation maps is the persistence of a dBOP spot around noon. During increased solar wind driving, the same two spots are conserved in Newell's map, with an additional region of increased broadband electron precipitation between 23 and 1 MLT. Additionally, the peak at dawn sees its intensity decreasing while it expands over a larger MLT region, now covering the noon region. The corresponding ($B_z < 0$) high-frequency dBOP shows a diffuse enhancement in all MLT sectors and is globally fainter compared to more quiet times. In these conditions, the highest dBOP probabilities are located in the dawn-to-noon region and in the midnight sector, similar to the broadband aurora. A similar comparison of the high-frequency dBOP maps with the Newell et al. (2009) maps for monoenergetic acceleration occurrence probability (their Figure 11) shows poor correlation.

From this comparison analysis, it is clear that dBOP and POP distributions show significant differences, suggesting that not all features captured in the POP are neces-

sarily captured in the dBOP (and vice versa), highlighting inherent differences between electron precipitation and magnetic field fluctuations. Based on these differences it is not expected that the two quantities exhibit identical morphologies. Nonetheless, we have shown that the POP and the dBOP, especially at low frequencies, present outstanding similarities such as the morphological asymmetric pattern with the dawn preference, and the response to the geomagnetic conditions. This suggests that some of the properties of the precipitation auroral oval can be inferred from the magnetic field perturbations, and it thus seems reasonable to use the low-frequency dBOP as a proxy for the auroral oval.

5 Conclusion

We have presented a method for investigating the auroral morphology using magnetic field perturbation data from Swarm/VFM. We implemented the dBOP at low 0.1–1 Hz and high 2.5–5 Hz frequencies and used it to assess the probability of observing disturbances in the magnetic field at auroral latitudes, as a function of magnetic latitude and local time. We found the dBOP global morphology to be strongly dependent on the investigated frequency range. At low frequencies, we have pointed out an asymmetric pattern between the dawn and dusk sectors, with a clear tendency for the dBOP to be more pronounced towards dawn (approx 5–8 MLT). At higher frequencies, the asymmetry in the dBOP is strongest near the noon-midnight meridian, with a large predominance of the dayside, especially the post-noon region. We also highlighted the reduced asymmetric pattern during geomagnetically disturbed conditions.

We discussed these results in the context of a previous study (Decotte et al., 2023) about the auroral electron precipitation occurrence probability (POP) and found that the low-frequency dBOP evinces spatial/morphological similarities with the POP. In particular, we observed an asymmetric pattern in both the POP and the low-frequency dBOP, with an unequivocal preference for the dawn-to-noon MLT sector. We also showed that the dBOP morphology is stable with varying detection thresholds and that the dawn-dusk asymmetry appears in all low-frequency distributions independent of IMF orientation and substorm phase, just as in the POP. This suggests that, like the POP in the energy range 1–30 keV, the dBOP below 1 Hz can be used as a proxy for the auroral oval, and a footprint of the large-scale circulation of plasma and magnetic flux in the magnetosphere.

Open Research Section

The Level 1B magnetic Swarm products are directly accessible through the Virtual environments for Earth Scientists (VirES) platform at `https://vires.services/`, either via the Swarm web user interface or via the VirES server API using an alternative client such as the Python client `https://doi.org/10.5281/zenodo.2554162`. The OMNI data, including the solar wind data and geomagnetic activity indices, are available on the NASA/GSFC SPDF interface at `http://spdf.gsfc.nasa.gov/pub/data/omni/high_res_omni/`.

Acknowledgments

This study was funded by the Trond Mohn Foundation, and by the Research Council of Norway through contracts 223252/F50 and 300844/F50.

We acknowledge the use of the Python tool VirES for Swarm to access the core data of this study, and we thank J.H. King and N.E. Papitashvili for the multi-sources OMNI data. We acknowledge the use of NASA/GSFC SPDF service to obtain these data. We also acknowledge the substorm timing list identified by the Ohtani and Gjerloev tech-

nique (Ohtani and Gjerloev, 2020), the SMU and SML indices (Newell and Gjerloev, 2011); and the SuperMAG collaboration (Gjerloev et al. 2012).

References

Burrell, A. G., Chisham, G., Milan, S. E., Kilcommons, L., Chen, Y. J., Thomas, E. G., & Anderson, B. (2020). AMPERE polar cap boundaries. *Annales Geophysicae*, *38*(2), 481–490. doi: 10.5194/angeo-38-481-2020

Carbary, J. F., Sotirelis, T., Newell, P. T., & Meng, C. I. (2003). Auroral boundary correlations between UVI and DMSP. *Journal of Geophysical Research: Space Physics*, *108*(A1). doi: 10.1029/2002JA009378

Chaston, C. C., Bonnell, J. W., Carlson, C. W., McFadden, J. P., Ergun, R. E., Strangeway, R. J., & Lund, E. J. (2004). Auroral ion acceleration in dispersive Alfvén waves. *Journal of Geophysical Research: Space Physics*, *109*(A4), 1–13. doi: 10.1029/2003JA010053

Chisham, G., Burrell, A. G., Thomas, E. G., & Chen, Y. J. (2022). Ionospheric Boundaries Derived From Auroral Images. *Journal of Geophysical Research: Space Physics*, *127*(7), 1–19. doi: 10.1029/2022JA030622

Christiansen, F., Papitashvili, V. O., & Neubert, T. (2002). Seasonal variations of high-latitude field-aligned currents inferred from Ørsted and Magsat observations. *Journal of Geophysical Research: Space Physics*, *107*(A2). doi: 10.1029/2001JA900104

Cowley, S., & Lockwood, M. (1992). Excitation and decay of solar-wind driven flows in the magnetosphere-ionosphere system. *Annales Geophysicae*.

Decotte, M., Laundal, K. M., Hatch, S. M., & Reistad, J. P. (2023, 6). Auroral Oval Morphology: Dawn-Dusk Asymmetry Partially Induced by Earth's Rotation. *Journal of Geophysical Research: Space Physics*, *128*(6), e2023JA031345. Retrieved from `https://onlinelibrary.wiley.com/doi/full/10.1029/2023JA031345https://onlinelibrary.wiley.com/doi/abs/10.1029/2023JA031345https://agupubs.onlinelibrary.wiley.com/doi/10.1029/2023JA031345` doi: 10.1029/2023JA031345

Dombeck, J., Cattell, C., Prasad, N., Meeker, E., Hanson, E., & McFadden, J. (2018). Identification of Auroral Electron Precipitation Mechanism Combinations and Their Relationships to Net Downgoing Energy and Number Flux. *Journal of Geophysical Research: Space Physics*, *123*(12), 064–10. doi: 10.1029/2018JA025749

Dungey, J. W. (1961, 1). Interplanetary Magnetic Field and the Auroral Zones. *Phys. Rev. Lett.*, *6*(2), 47–48. Retrieved from `https://link.aps.org/doi/10.1103/PhysRevLett.6.47` doi: 10.1103/PhysRevLett.6.47

Fujii, R., Oguti, T., & Yamamoto, T. (1985, 7). Relationships between pulsating auroras and field-aligned electric currents. *National Institute Polar Research Memoirs*, *36*.

Gillies, D. M., Knudsen, D., Spanswick, E., Donovan, E., Burchill, J., & Patrick, M. (2015, 11). Swarm observations of field-aligned currents associated with pulsating auroral patches. *Journal of Geophysical Research: Space Physics*, *120*(11), 9484–9499. Retrieved from `https://onlinelibrary.wiley.com/doi/full/10.1002/2015JA021416https://onlinelibrary.wiley.com/doi/abs/10.1002/2015JA021416https://agupubs.onlinelibrary.wiley.com/doi/10.1002/2015JA021416` doi: 10.1002/2015JA021416

Hatch, S. M., Haaland, S., Laundal, K. M., Moretto, T., Yau, A. W., Bjoland, L., ... Oksavik, K. (2020). Seasonal and Hemispheric Asymmetries of F Region Polar Cap Plasma Density: Swarm and CHAMP Observations. *Journal of Geophysical Research: Space Physics*, *125*(11). doi: 10.1029/2020JA028084

Hatch, S. M., LaBelle, J., Lotko, W., Chaston, C. C., & Zhang, B. (2017). IMF Control of Alfvénic Energy Transport and Deposition at High Latitudes. *Journal*

of Geophysical Research: Space Physics, *122*(12), 12189–12211. doi: 10.1002/2017JA024175

Hatch, S. M., Laundal, K. M., & Reistad, J. P. (2022, 9). Testing the mirror symmetry of Birkeland and ionospheric currents with respect to magnetic latitude, dipole tilt angle, and IMF B y. *Frontiers in Astronomy and Space Sciences*, *9*, 958977. doi: 10.3389/FSPAS.2022.958977/BIBTEX

Hatch, S. M., Moretto, T., Lynch, K. A., Laundal, K. M., Gjerloev, J. W., & Lund, E. J. (2020). The Relationship Between Cusp Region Ion Outflows and East-West Magnetic Field Fluctuations at 4,000-km Altitude. *Journal of Geophysical Research: Space Physics*, *125*(3), 1–18. doi: 10.1029/2019JA027454

Iijima, T., & Potemra, T. A. (1976). The amplitude distribution of field-aligned currents at northern high latitudes observed by Triad. *Journal of Geophysical Research*, *81*(13), 2165–2174. doi: 10.1029/ja081i013p02165

Iijima, T., & Potemra, T. A. (1978). Large-scale characteristics of field-aligned currents associated with substorms. *Journal of Geophysical Research*, *83*(A2), 599. doi: 10.1029/ja083ia02p00599

Juusola, L., Vanhamäki, H., Viljanen, A., & Smirnov, M. (2020, 9). Induced currents due to 3D ground conductivity play a major role in the interpretation of geomagnetic variations. *Annales Geophysicae*, *38*(5), 983–998. doi: 10.5194/ANGEO-38-983-2020

Kamide, Y., Richmond, A. D., & Matsushita, S. (1981). Estimation of ionospheric electric fields, ionospheric currents, and field-aligned currents from ground magnetic records. *Journal of Geophysical Research*, *86*(A2), 801. doi: 10.1029/ja086ia02p00801

Kauristie, K., Weygand, J., Pulkkinen, T. I., Murphree, J. S., & Newell, P. T. (1999, 2). Size of the auroral oval: UV ovals and precipitation boundaries compared. *Journal of Geophysical Research: Space Physics*, *104*(A2), 2321–2331. Retrieved from `https://onlinelibrary.wiley.com/doi/full/10.1029/1998JA900046https://onlinelibrary.wiley.com/doi/abs/10.1029/1998JA900046https://agupubs.onlinelibrary.wiley.com/doi/10.1029/1998JA900046` doi: 10.1029/1998JA900046

Khazanov, G. V., & Glocer, A. (2020). How Magnetically Conjugate Atmospheres and the Magnetosphere Participate in the Formation of Low-Energy Electron Precipitation in the Region of Diffuse Aurora. *Journal of Geophysical Research: Space Physics*, *125*(8), 1–15. doi: 10.1029/2020JA028057

Kilcommons, L. M., Redmon, R. J., & Knipp, D. J. (2017a). A new DMSP magnetometer and auroral boundary data set and estimates of field-aligned currents in dynamic auroral boundary coordinates. *Journal of Geophysical Research: Space Physics*, *122*(8), 9068–9079. doi: 10.1002/2016JA023342

Kilcommons, L. M., Redmon, R. J., & Knipp, D. J. (2017b). A new DMSP magnetometer and auroral boundary data set and estimates of field-aligned currents in dynamic auroral boundary coordinates. *Journal of Geophysical Research: Space Physics*, *122*(8), 9068–9079. Retrieved from `https://agupubs.onlinelibrary.wiley.com/doi/abs/10.1002/2016JA023342` doi: https://doi.org/10.1002/2016JA023342

King, J. H., & Papitashvili, N. E. (2005, 2). Solar wind spatial scales in and comparisons of hourly Wind and ACE plasma and magnetic field data. *Journal of Geophysical Research: Space Physics*, *110*(A2), 2104. Retrieved from `https://onlinelibrary.wiley.com/doi/full/10.1029/2004JA010649https://onlinelibrary.wiley.com/doi/abs/10.1029/2004JA010649https://agupubs.onlinelibrary.wiley.com/doi/10.1029/2004JA010649` doi: 10.1029/2004JA010649

Kustov, A. V., Lyatsky, W. B., Sofko, G. J., & Xu, L. (2000). Field-aligned currents in the polar cap at small IMF Bz and By inferred from SuperDARN radar observations. *Journal of Geophysical Research: Space Physics*, *105*(A1), 205–214.

778 doi: 10.1029/1999ja900428
779 Laundal, K. M., Finlay, C. C., Olsen, N., & Reistad, J. P. (2018, 5). Solar Wind
780 and Seasonal Influence on Ionospheric Currents From Swarm and CHAMP
781 Measurements. *Journal of Geophysical Research: Space Physics*, *123*(5),
782 4402–4429. Retrieved from https://onlinelibrary.wiley.com/doi/
783 full/10.1029/2018JA025387https://onlinelibrary.wiley.com/doi/
784 abs/10.1029/2018JA025387https://agupubs.onlinelibrary.wiley.com/
785 doi/10.1029/2018JA025387 doi: 10.1029/2018JA025387
786 Laundal, K. M., OØstgaard, N., Frey, H. U., & Weygand, J. M. (2010). Seasonal
787 and interplanetary magnetic field-dependent polar cap contraction during
788 substorm expansion phase. *Journal of Geophysical Research: Space Physics*,
789 *115*(11), 1–12. doi: 10.1029/2010JA015910
790 Laundal, K. M., & Richmond, A. D. (2017). Magnetic Coordinate Systems. *Space*
791 *Science Reviews*, *206*(1), 27–59. Retrieved from https://doi.org/10.1007/
792 s11214-016-0275-y doi: 10.1007/s11214-016-0275-y
793 Lühr, H., Kervalishvili, G. N., Stolle, C., Rauberg, J., & Michaelis, I. (2019, 12).
794 Average Characteristics of Low-Latitude Interhemispheric and F Region
795 Dynamo Currents Deduced From the Swarm Satellite Constellation. *Jour-*
796 *nal of Geophysical Research: Space Physics*, *124*(12), 10631–10644. doi:
797 10.1029/2019JA027419
798 Milan, S. E., Clausen, L. B., Coxon, J. C., Carter, J. A., Walach, M. T.,
799 Laundal, K., ... Anderson, B. J. (2017). Overview of Solar
800 Wind–Magnetosphere–Ionosphere–Atmosphere Coupling and the Genera-
801 tion of Magnetospheric Currents. *Space Science Reviews*, *206*(1-4), 547–573.
802 Retrieved from http://dx.doi.org/10.1007/s11214-017-0333-0 doi:
803 10.1007/s11214-017-0333-0
804 Nagatsuma, T., Fukunishi, H., Hayakawa, H., Mukai, T., & Matsuoka, A. (1996,
805 10). Field-aligned currents associated with Alfven waves in the pole-
806 ward boundary region of the nightside auroral oval. *Journal of Geophys-*
807 *ical Research: Space Physics*, *101*(A10), 21715–21729. Retrieved from
808 https://onlinelibrary.wiley.com/doi/full/10.1029/96JA01797https://
809 onlinelibrary.wiley.com/doi/abs/10.1029/96JA01797https://
810 agupubs.onlinelibrary.wiley.com/doi/10.1029/96JA01797 doi:
811 10.1029/96JA01797
812 Nagatsuma, T., Fukunishi, H., & Mukai, T. (1995, 2). Spatial relationships
813 between field-aligned currents and suprathermal electron beams observed
814 at the poleward boundary of the nightside auroral oval. *Journal of Geo-*
815 *physical Research: Space Physics*, *100*(A2), 1625–1637. Retrieved from
816 https://onlinelibrary.wiley.com/doi/full/10.1029/94JA02440https://
817 onlinelibrary.wiley.com/doi/abs/10.1029/94JA02440https://
818 agupubs.onlinelibrary.wiley.com/doi/10.1029/94JA02440 doi:
819 10.1029/94JA02440
820 Neubert, T., & Christiansen, F. (2003, 10). Small-scale, field-aligned currents
821 at the top-side ionosphere. *Geophysical Research Letters*, *30*(19). Re-
822 trieved from https://onlinelibrary.wiley.com/doi/full/10.1029/
823 2003GL017808https://onlinelibrary.wiley.com/doi/abs/10.1029/
824 2003GL017808https://agupubs.onlinelibrary.wiley.com/doi/10.1029/
825 2003GL017808 doi: 10.1029/2003GL017808
826 Newell, P. T., Feldstein, Y. I., Galperin, Y. I., & Meng, C.-I. (1996). Morphol-
827 ogy of nightside precipitation. *Journal of Geophysical Research: Space Physics*,
828 *101*(A5), 10737–10748. doi: 10.1029/95ja03516
829 Newell, P. T., Liou, K., Zhang, Y., Sotirelis, T., Paxton, L. J., & Mitchell,
830 E. J. (2014). OVATION Prime-2013: Extension of auroral precipitation
831 model to higher disturbance levels. *Space Weather*, *12*(6), 368–379. doi:
832 10.1002/2014SW001056

Newell, P. T., Ruohoniemi, J. M., & Meng, C.-I. (2004a). Maps of precipitation by source region, binned by IMF, with inertial convection streamlines. *Journal of Geophysical Research: Space Physics*, *109*(A10). Retrieved from `https://agupubs.onlinelibrary.wiley.com/doi/abs/10.1029/2004JA010499` doi: https://doi.org/10.1029/2004JA010499

Newell, P. T., Ruohoniemi, J. M., & Meng, C. I. (2004b). Maps of precipitation by source region, binned by IMF, with inertial convection streamlines. *Journal of Geophysical Research: Space Physics*, *109*(A10), 1–20. doi: 10.1029/2004JA010499

Newell, P. T., Sotirelis, T., Liou, K., Meng, C. I., & Rich, F. J. (2007). A nearly universal solar wind-magnetosphere coupling function inferred from 10 magnetospheric state variables. *Journal of Geophysical Research: Space Physics*, *112*(1), 1–16. doi: 10.1029/2006JA012015

Newell, P. T., Sotirelis, T., & Wing, S. (2009). Diffuse, monoenergetic, and broadband aurora: The global precipitation budget. *Journal of Geophysical Research: Space Physics*, *114*(A9). Retrieved from `https://agupubs.onlinelibrary.wiley.com/doi/abs/10.1029/2009JA014326` doi: https://doi.org/10.1029/2009JA014326

Ohma, A., Laundal, K. M., Madelaire, M., Hatch, S. M., Gasparini, S., Reistad, J. P., ... Decotte, M. (2023). Excitation and decay of the auroral oval. *JGR: Space Physics*. doi: 10.22541/essoar.169447428.84472457/v1

Ohtani, S., & Gjerloev, J. W. (2020). Is the Substorm Current Wedge an Ensemble of Wedgelets?: Revisit to Midlatitude Positive Bays. *Journal of Geophysical Research: Space Physics*, *125*(9), e2020JA027902. Retrieved from `https://agupubs.onlinelibrary.wiley.com/doi/abs/10.1029/2020JA027902` doi: https://doi.org/10.1029/2020JA027902

Redmon, R. J., Peterson, W. K., Andersson, L., Kihn, E. A., Denig, W. F., Hairston, M., & Coley, R. (2010). Vertical thermal O+ flows at 850 km in dynamic auroral boundary coordinates. *Journal of Geophysical Research: Space Physics*, *115*(11), 1–10. doi: 10.1029/2010JA015589

Richmond, A. D. (1995). Ionospheric Electrodynamics Using Magnetic Apex Coordinates. *Journal of geomagnetism and geoelectricity*, *47*(2), 191–212. doi: 10.5636/jgg.47.191

Ritter, P., Lühr, H., & Rauberg, J. (2013). Determining field-aligned currents with the Swarm constellation mission. *Earth, Planets and Space*, *65*(11), 1285–1294. doi: 10.5047/eps.2013.09.006

Robinson, R. M., Zhang, Y., Anderson, B. J., Zanetti, L. J., Korth, H., & Fitzmaurice, A. (2018). Statistical Relations Between Field-Aligned Currents and Precipitating Electron Energy Flux. *Geophysical Research Letters*, *45*(17), 8738–8745. doi: 10.1029/2018GL078718

Sato, N., Wright, D. M., Carlson, C. W., Ebihara, Y., Sato, M., Saemundsson, T., ... Lester, M. (2004). Generation region of pulsating aurora obtained simultaneously by the FAST satellite and a Syowa-Iceland conjugate pair of observatories. *Journal of Geophysical Research: Space Physics*, *109*(A10). doi: 10.1029/2004JA010419

Smith, A. R. A., & Pačes, M. (2022). Python tools for ESA's Swarm mission: VirES for Swarm and surrounding ecosystem. *Frontiers in Astronomy and Space Sciences*, *9*(October), 1–10. doi: 10.3389/fspas.2022.1002697

Stasiewicz, K., Bellan, P., Chaston, C., Kletzing, C., Lysak, R., Maggs, J., ... Wahlund, J. E. (2000). Small scale Alfvenic structure in the aurora. *Space Science Reviews*, *92*(3-4), 423–533. Retrieved from `https://link.springer.com/article/10.1023/A:1005207202143` doi: 10.1023/A:1005207202143/METRICS

Strangeway, R. J., Elphic, R. C., Peria, W. J., & Carlson, C. W. (2000). FAST Observations of Electromagnetic Stresses Applied to the Polar Ionosphere.

Geophysical Monograph Series, *118*, 21–29. Retrieved from https://onlinelibrary.wiley.com/doi/full/10.1029/GM118p0021https://onlinelibrary.wiley.com/doi/abs/10.1029/GM118p0021https://agupubs.onlinelibrary.wiley.com/doi/10.1029/GM118p0021 doi: 10.1029/GM118P0021

Thayer, J. P., & Semeter, J. (2004). The convergence of magnetospheric energy flux in the polar atmosphere. *Journal of Atmospheric and Solar-Terrestrial Physics*, *66*(10), 807–824. doi: 10.1016/j.jastp.2004.01.035

Xiong, C., & Lühr, H. (2014). An empirical model of the auroral oval derived from CHAMP field-aligned current signatures - Part 2. *Annales Geophysicae*, *32*(6), 623–631. doi: 10.5194/angeo-32-623-2014

Xiong, C., Lühr, H., Wang, H., & Johnsen, M. G. (2014). Determining the boundaries of the auroral oval from CHAMP field-aligned current signatures – Part 1. *Annales Geophysicae*, *32*(6), 609–622. Retrieved from https://angeo.copernicus.org/articles/32/609/2014/ doi: 10.5194/angeo-32-609-2014

Xiong, C., Stolle, C., Alken, P., & Rauberg, J. (2020). Relationship between large-scale ionospheric field-aligned currents and electron/ion precipitations: DMSP observations. *Earth, Planets and Space*, *72*(1). Retrieved from https://doi.org/10.1186/s40623-020-01286-z doi: 10.1186/s40623-020-01286-z

Zhang, Y., & Paxton, L. J. (2008). An empirical Kp-dependent global auroral model based on TIMED/GUVI FUV data. *Journal of Atmospheric and Solar-Terrestrial Physics*, *70*(8-9), 1231–1242. doi: 10.1016/j.jastp.2008.03.008